JGR Biogeosciences

RESEARCH ARTICLE
10.1029/2020JG005787

Attribution of Land-Use/Land-Cover Change Induced Surface Temperature Anomaly: How Accurate Is the First-Order Taylor Series Expansion?

Chi Chen[1], **Liang Wang**[1], **Ranga B. Myneni**[1], **and Dan Li**[1]

[1]Department of Earth and Environment, Boston University, Boston, MA, USA

Key Points:
- The accuracy of land surface temperature and its attribution is affected by the order of Taylor series expansion
- First-order Taylor series expansion suffices for obtaining an analytical form of land surface temperature
- Second-order Taylor series expansion is recommended for the attribution model, especially for large surface disturbances

Supporting Information:
- Supporting Information S1

Correspondence to:
C. Chen and D. Li,
chenchi@bu.edu;
lidan@bu.edu

Citation:
Chen, C., Wang, L., Myneni, R. B., & Li, D. (2020). Attribution of land-use/land-cover change induced surface temperature anomaly: How accurate is the first-order Taylor series expansion? *Journal of Geophysical Research: Biogeosciences*, *125*, e2020JG005787. https://doi.org/10.1029/2020JG005787

Received 15 APR 2020
Accepted 28 AUG 2020
Accepted article online 8 SEP 2020

Abstract Land surface temperature (LST) responds to land-use/land-cover change (LULCC), which modifies surface properties that control the surface energy balance (SEB). Quantifying changes in LST due to individual perturbations caused by LULCC is an attribution problem. Most attribution methods are based on the first-order Taylor series expansion (FOTSE) of a linearized SEB equation. The accuracy of these methods is affected by the use of FOTSE at two places. The first is to linearize the SEB equation and to obtain an analytical solution for LST (the LST model), and the second is to obtain LST changes as the linear sum of concurrent changes in multiple factors (the attribution model). In this study, we systematically assess the importance of non-linear effects lost in these linearization processes using the second-order Taylor series expansion (SOTSE). Results show that while the SOTSE LST model outperforms the FOTSE LST model, the order of Taylor series expansion in the LST model does not significantly influence the attribution of LST changes. However, the SOTSE attribution model is considerably more accurate than the FOTSE attribution model, especially when the magnitude of perturbations is large. Results suggest that contributions from higher-order and cross-order terms in the attribution model can be as large as 50%. Sensitivity analysis further shows that non-linear effects associated with changing surface resistance for LULCC scenarios with large perturbations (e.g., deforestation and urbanization) are particularly strong. In conclusion, we recommend using the FOTSE LST model and the SOTSE attribution model.

Plain Language Summary Land-use/land-cover change can modify the land surface temperature. It is critical to quantify such effects especially under the changing climate. The observed changes in land surface temperate are a combined effect of changing multiple biophysical factors. Thus, parsing the changes in land surface temperature due to land-use/land-cover change is an attribution problem. Most analytical attribution methods tackle this problem by approximations, where the first-order Taylor series expansion is used twice. One is to obtain an analytical solution of land surface temperature from the energy balance equation, and the other is to attribute the changes in land surface temperature to different factors, which assumes the attributable factors are independent. In this study, we assess how accurate the first-order Taylor series expansions are. Our analyses show that the analytical form of land surface temperature obtained by the first-order Taylor series expansion is adequate and not a primary factor impacting the accuracy of the attribution. However, we recommend using second-order Taylor series expansion in attributing the changes in land surface temperature, especially for large disturbances such as deforestation and urbanization. Our analyses also suggest that under large disturbances, the attributable factors are not independent.

1. Introduction

Land surface temperature (LST), or the radiometric skin temperature, is an important variable describing the status of the surface energy equilibrium in the Earth system (Monteith & Unsworth, 2007). Changes in LST have multitude of implications such as creating the so-called urban heat islands (Li et al., 2019), affecting human mortality during heat waves (Li & Bou-Zeid, 2013), and changing ecosystem carbon uptake (Keenan et al., 2016) and agricultural yields (Li et al., 2020; Zhao et al., 2017). Land-use/land-cover change (LULCC) is one major forcing that directly alters the LST by modifying multiple surface biophysical factors controlling the surface energy balance (SEB) (Alkama & Cescatti, 2016; Bonan, 2008; Bright et al., 2017; Mahmood et al., 2013; Pielke et al., 2011). For example, Duveiller et al. (2018) estimated that vegetation

cover change from 2000 to 2015, including deforestation (i.e., relatively large disturbances), has led to a global average increase in LST by 0.23°C. Zeng et al. (2017) found that the recent increase of leaf area index (a.k.a. Earth greening, which is one type of small disturbances) offsets the rising trend of near-surface air temperature by 0.03°C per decade. Therefore, a better understanding of the effects of LULCC on LST can contribute to policy development on combating global warming.

Quantifying changes in LST due to individual perturbations caused by LULCC is essentially an attribution problem. There is a surge of models attributing surface temperature anomalies induced by LULCC to different surface biophysical factors based on the first-order Taylor series expansion (FOTSE) of a linearized SEB equation (Burakowski et al., 2018; Chen & Dirmeyer, 2016; Devaraju et al., 2018; Ge et al., 2019; Juang et al., 2007; Lee et al., 2011; Li et al., 2019; Liao et al., 2018; Luyssaert et al., 2014; Moon et al., 2020; Rigden & Li, 2017; Zeng et al., 2017; Zhao, Lee, & Schultz, 2017; Zhao et al., 2014). The accuracy of these methods is determined by the use of FOTSE at two places. The first is to linearize the non-linear terms in the SEB equation and to obtain an exact solution for LST (denoted as the LST model). Examples of these non-linear terms are the outgoing longwave radiation and the saturation specific humidity. The second is to obtain the changes in LST as the linear sum of concurrent changes in multiple surface biophysical factors (denoted as the attribution model). In other words, the attribution model implicitly assumes that the attributable factors are independent (hereafter "independence assumption") by neglecting higher-order and cross-order terms. Similar use of FOTSE for attributing changes in other quantities such as evapotranspiration based on simple model schemes like the Penman and Penman-Monteith equations (Roderick et al., 2007; Yang & Yang, 2011) or the Budyko framework (Wang & Hejazi, 2011; Xu et al., 2014; Zhang et al., 2016) can be also found in the literature.

It is unclear whether and under what conditions the non-linear effects neglected in these linearization processes become important. Mathematically, the accuracy of FOTSE decreases as the perturbation becomes larger. In this particular problem, given that the first FOTSE is conducted around the air temperature (in the LST model) and the second FOTSE is conducted around the reference surface temperature (in the attribution model), it is expected that the accuracy of these models decreases as the LST departs from the air temperature (Paw U & Gao, 1988; Tracy et al., 1984) or as the LULCC disturbances are large (e.g., deforestation).

In this study, we systematically assess the importance of non-linear effects lost in these linearization processes by using second-order Taylor series expansion (SOTSE). We conduct these analyses based on an attribution framework called two-resistance mechanism (TRM) method (Rigden & Li, 2017). The TRM method has been widely used in studying the temperature anomalies caused by deforestation (Liao et al., 2018), urbanization (Li et al., 2019), heat waves (Wang et al., 2019), and vegetation phenology (Moon et al., 2020). Based on the TRM method, we compare the accuracy of the LST models with FOTSE and SOTSE. Furthermore, based on the LST models, we evaluate the biases of the attribution models with FOTSE and SOTSE. This paper is organized as follows: Section 2 describes the TRM method and the mathematical derivations of the LST model and the attribution model with FOTSE and SOTSE; section 3 presents the results and discusses the LST models and attribution models with different orders of Taylor series expansion; section 4 summarizes the study.

2. Materials and Methods

2.1. Two-Resistance Mechanism Method

The original TRM method attributes changes in LST due to disturbances to (1) changes in surface factors such as albedo, aerodynamic resistance, surface resistance, surface emissivity, and ground heat flux and to (2) changes in atmospheric conditions such as air temperature and humidity, incoming shortwave and longwave radiation (Liao et al., 2018; Moon et al., 2020; Rigden & Li, 2017; Wang et al., 2019). In this study, we assume that all atmospheric conditions are defined above the blending height and thus are not affected by LULCC at the surface (Lee et al., 2011; Rigden & Li, 2017). The implication of this assumption will be discussed later. To make the derivations both concise and practically instructive, only the first three surface factors are considered: albedo (α), aerodynamic resistance (r_a), and surface resistance (r_s) (Liao et al., 2018; Rigden & Li, 2017). For these three biophysical factors directly affected by LULCC, albedo controls the shortwave radiation remaining in the surface; aerodynamic resistance regulates the efficiency of the turbulent transports of heat and water vapor between the land and the atmosphere; surface resistance is the

additional resistance to water vapor during its transport through the pores on leaves (stomata) or in the soil. We emphasize that the primary goal of this study is to evaluate the performance of different orders of Taylor series expansion in the TRM method instead of applying the TRM method to specific problems.

Within the TRM attribution framework, Taylor's theorem is used twice: (1) The first use of Taylor's theorem is to solve LST from the SEB equation, which is a univariate Taylor series expansion (i.e., T_s); (2) the second use of Taylor's theorem is to attribute changes in LST to changes in biophysical factors (e.g., α, r_a, and r_s), which is a multivariate Taylor series expansion. The details are described through sections 2.1 to 2.6.

To begin with, the SEB equation is expressed as

$$R_n = S_{in}(1-\alpha) + \varepsilon L_{in} - \varepsilon\sigma {T_s}^4 = H + LE + G, \tag{1}$$

where R_n is the net radiation (W m^{-2}), S_{in} and L_{in} are the incoming shortwave and the longwave radiation (W m^{-2}), respectively, α and ε are the albedo and the surface emissivity (dimensionless), respectively, H and LE are the sensible and the latent heat fluxes (W m^{-2}), respectively, T_s is the LST (K), $\varepsilon\sigma {T_s}^4$ is the outgoing longwave radiation where σ is the Stefan-Boltzmann constant (5.670367×10^{-8} W m^{-2} K^{-4}), and G is the ground heat flux (W m^{-2}). In the TRM method, G is treated as a forcing instead of an internal variable and thus is not a function of T_s. This strategy of handling G is similar to the so-called Penman equation (Monteith & Unsworth, 2007). If G were treated as an internal variable, it would be a non-linear function of T_s; for example, it follows the Fourier's law.

Further connecting H and LE with T_s through the aerodynamic resistance and surface resistance concepts gives (Brutsaert, 2005, 2013; Monteith & Unsworth, 2007)

$$H = \frac{\rho c_p}{r_a}(T_s - T_a), \tag{2}$$

$$LE = \frac{\rho L_v}{r_a + r_s}\left[q_s^*(T_s) - q_a\right], \tag{3}$$

where ρ is the air density (kg m^{-3}), c_p is the specific heat of air at constant pressure (1,004.64 J kg^{-1} K^{-1}), L_v is the latent heat of vaporization (2.4665×10^6 J kg^{-1}) or sublimation (2.8002×10^6 J kg^{-1}), T_a is the air potential temperature (K), $q_s^*(T_s)$ is the saturation specific humidity at the surface temperature (g kg^{-1}), and q_a is the air specific humidity (g kg^{-1}). Substituting Equations 2 and 3 into Equation 1 results in a non-linear equation for T_s:

$$S_{in}(1-\alpha) + \varepsilon L_{in} - \varepsilon\sigma {T_s}^4 = \frac{\rho c_p}{r_a}(T_s - T_a) + \frac{\rho L_v}{r_a + r_s}\left[q_s^*(T_s) - q_a\right] + G. \tag{4}$$

2.2. FOTSE (Linear Approximation) of Non-linear Terms With LST

To obtain an analytical form of T_s, non-linear terms (i.e., outgoing longwave radiation and the saturation specific humidity) are linearized by FOTSE at the point T_a, which gives

$$\varepsilon\sigma {T_s}^4 \approx \varepsilon\sigma {T_a}^4 + 4\varepsilon\sigma {T_a}^3(T_s - T_a), \tag{5}$$

$$q_s^*(T_s) \approx q_a^*(T_a) + \left.\frac{\partial q^*}{\partial T}\right|_{T_a}(T_s - T_a). \tag{6}$$

Substituting Equations 5 and 6 into Equation 4, one arrives at an analytical solution for T_s:

$$T_s = \frac{\lambda_o^{'}\left[R_n^* - G - \dfrac{\rho L_v\left(q_a^*(T_a) - q_a\right)}{(r_a + r_s)}\right]}{f} + T_a, \tag{7}$$

where

$$R_n^* = S_{in}(1-\alpha) + \varepsilon L_{in} - \varepsilon\sigma {T_a}^4,$$

$$f = \frac{1}{r_o} + \frac{1}{r_a}\left[1 + \frac{\Delta}{\gamma}\left(\frac{r_a}{r_a + r_s}\right)\right],$$

$$\Delta = \left.\frac{\partial e^*}{\partial T}\right|_{T_a},$$

$$r_o = \frac{\rho c_p}{4\varepsilon\sigma {T_a}^3},$$

$$\gamma = \frac{c_p P}{0.622 L_v},$$

$$\lambda_o^{'} = \frac{1}{\rho c_p},$$

and $e^* = 611 \times e^{\frac{17.27(273.15 - T)}{T - 35.85}}$ is the saturation vapor pressure (Pa) (Dingman, 2008), $q^* = \frac{0.622 e^*}{P}$ and P is the atmospheric pressure (Pa) at the surface.

2.3. SOTSE (Quadratic Approximation) of Non-linear Terms With LST

Similarly, one can use SOTSE to approximate the non-linear terms with T_s at point T_a, as follows:

$$\epsilon\sigma {T_s}^4 \approx \varepsilon\sigma {T_a}^4 + 4\varepsilon\sigma {T_a}^3 (T_s - T_a) + 6\varepsilon\sigma {T_a}^2 (T_s - T_a)^2, \tag{8}$$

$$q_s^*(T_s) \approx q_a^*(T_a) + \left.\frac{\partial q^*}{\partial T}\right|_{T_a} (T_s - T_a) + \left.\frac{1\partial^2 q^*}{2\partial T^2}\right|_{T_a} (T_s - T_a)^2. \tag{9}$$

Substituting Equations 8 and 9 into Equation 4 and rearranging yield a quadratic equation with only one unknown, T_s:

$$a(T_s - T_a)^2 + b(T_s - T_a) + c = 0, \tag{10}$$

where

$$a = 6\varepsilon\sigma {T_a}^2 + \left.\frac{1\partial^2 q^*}{2\partial T^2}\right|_{T_a},$$

$$b = 4\varepsilon\sigma {T_a}^3 + \frac{\rho L_v \left.\frac{\partial q^*}{\partial T}\right|_{T_a}}{(r_a + r_s)} + \frac{\rho c_p}{r_a},$$

$$c = \frac{\rho L_v \left(q_a^*(T_a) - q_a\right)}{(r_a + r_s)} - \left(R_n^* - G\right).$$

Solving Equation 10 gives two roots for T_s. Since T_s must be above zero Kelvin, only the positive root is physically meaningful, as shown in Equation 11:

$$T_s = \frac{-b + \sqrt{b^2 - 4ac}}{2a} + T_a. \tag{11}$$

2.4. Attribution of the Changes in LST Using FOTSE

As mentioned in section 2.1, in this study, we only consider changes in LST due to changes in three biophysical factors (i.e., α, r_a, and r_s). According to Taylor's theorem, the FOTSE to T_s can be written as

$$\Delta T_s = \left(\frac{\partial T_s}{\partial \alpha}\right)\Delta\alpha + \left(\frac{\partial T_s}{\partial r_a}\right)\Delta r_a + \left(\frac{\partial T_s}{\partial r_s}\right)\Delta r_s, \tag{12}$$

where Δ indicates a change; for example, ΔT_s is the change in LST. Each term on the right-hand side is called a contribution. The contribution terms consist of two parts: the partial derivatives (e.g., $\frac{\partial T_s}{\partial r_a}$) and the changes (e.g., Δr_a). The use of the FOTSE in the attribution model implicitly assumes that the contributions to the changes in LST from different factors are independent of each other (Rigden & Li, 2017).

2.5. Attribution of the Changes in LST Using SOTSE

The SOTSE to T_s can be written as

$$\begin{aligned}\Delta T_s = &\left(\frac{\partial T_s}{\partial \alpha}\right)\Delta\alpha + \left(\frac{\partial T_s}{\partial r_a}\right)\Delta r_a + \left(\frac{\partial T_s}{\partial r_s}\right)\Delta r_s \\ &+\frac{1}{2}\left[\left(\frac{\partial^2 T_s}{\partial \alpha^2}\right)(\Delta\alpha)^2 + \left(\frac{\partial^2 T_s}{\partial {r_a}^2}\right)(\Delta r_a)^2 + \left(\frac{\partial^2 T_s}{\partial {r_s}^2}\right)(\Delta r_s)^2 + 2\left(\frac{\partial^2 T_s}{\partial\alpha\partial r_a}\right)\Delta\alpha\Delta r_a\right. \\ &\left.+2\left(\frac{\partial^2 T_s}{\partial\alpha\partial r_s}\right)\Delta\alpha\Delta r_s + 2\left(\frac{\partial^2 T_s}{\partial r_a\partial r_s}\right)\Delta r_a\Delta r_s\right],\end{aligned} \tag{13}$$

where, on the right-hand side, the first three terms are the first-order terms that are identical to those in Equation 12; terms in the second row are the second-order terms; terms in the third row are the cross-order terms arising from the covariance of different attributable factors. The SOTSE attribution model partially considers non-linear effects lost in the FOTSE attribution model and, mathematically, no longer assumes the attributable factors are independent of each other.

2.6. Derivatives of LST to Biophysical Factors

The next step is to obtain the derivatives of LST to the three biophysical factors using the LST models with FOTSE and SOTSE described in sections 2.2 and 2.3, respectively.

With the linear approximation of LST (FOTSE LST model, Equation 7), one can derive the first-order derivatives of LST to biophysical factors, as follows:

$$\frac{\partial T_s}{\partial \alpha} = -\frac{\lambda_o^{'} S_{\text{in}}}{f}, \tag{14}$$

$$\frac{\partial T_s}{\partial r_a} = \frac{\lambda_o^{'}\rho L_v\left(q_a^*(T_a) - q_a\right)}{f(r_a + r_s)^2} + \frac{1}{f^2 {r_a}^2}\left[1 + \frac{\Delta}{\gamma}\left(\frac{r_a}{r_a + r_s}\right)^2\right]\left[R_n^* - G - \frac{\rho L_v\left(q_a^*(T_a) - q_a\right)}{(r_a + r_s)}\right], \tag{15}$$

$$\frac{\partial T_s}{\partial r_s} = \frac{\lambda_o^{'}\rho L_v\left(q_a^*(T_a) - q_a\right)}{f(r_a + r_s)^2} + \frac{\Delta}{f^2\gamma}\left(\frac{1}{r_a + r_s}\right)^2\left[R_n^* - G - \frac{\rho L_v\left(q_a^*(T_a) - q_a\right)}{(r_a + r_s)}\right]. \tag{16}$$

Similar to the linear approximation, one can derive the first-order derivatives of LST to biophysical factors based on the quadratic approximation of T_s (SOTSE LST model, Equation 11). Their derivatives are presented by using the chain rule of calculus, as follows:

$$\frac{\partial T_s}{\partial \alpha} = \left(\frac{\partial T_s}{\partial a}\right)\left(\frac{\partial a}{\partial \alpha}\right) + \left(\frac{\partial T_s}{\partial b}\right)\left(\frac{\partial b}{\partial \alpha}\right) + \left(\frac{\partial T_s}{\partial c}\right)\left(\frac{\partial c}{\partial \alpha}\right), \tag{17}$$

$$\frac{\partial T_s}{\partial r_a} = \left(\frac{\partial T_s}{\partial a}\right)\left(\frac{\partial a}{\partial r_a}\right) + \left(\frac{\partial T_s}{\partial b}\right)\left(\frac{\partial b}{\partial r_a}\right) + \left(\frac{\partial T_s}{\partial c}\right)\left(\frac{\partial c}{\partial r_a}\right), \tag{18}$$

$$\frac{\partial T_s}{\partial r_s} = \left(\frac{\partial T_s}{\partial a}\right)\left(\frac{\partial a}{\partial r_s}\right) + \left(\frac{\partial T_s}{\partial b}\right)\left(\frac{\partial b}{\partial r_s}\right) + \left(\frac{\partial T_s}{\partial c}\right)\left(\frac{\partial c}{\partial r_s}\right), \tag{19}$$

where

$$\frac{\partial T_s}{\partial a} = \frac{-b^2 + b\sqrt{b^2 - 4ac} + 2ac}{2a^2\sqrt{b^2 - 4ac}},$$

$$\frac{\partial T_s}{\partial b} = \frac{b - \sqrt{b^2 - 4ac}}{2a\sqrt{b^2 - 4ac}},$$

$$\frac{\partial T_s}{\partial c} = -\frac{1}{\sqrt{b^2 - 4ac}},$$

$$\frac{\partial a}{\partial \alpha} = \frac{\partial b}{\partial \alpha} = 0,$$

$$\frac{\partial a}{\partial r_a} = \frac{\partial a}{\partial r_s} = -\frac{1}{2\gamma}\frac{\partial^2 e^*}{\partial T^2}\bigg|_{T_a}\frac{1}{(r_a + r_s)^2},$$

$$\frac{\partial b}{\partial r_a} = -\frac{1}{{r_a}^2}\left[1 + \frac{\Delta}{\gamma}\left(\frac{r_a}{r_a + r_s}\right)^2\right],$$

$$\frac{\partial b}{\partial r_s} = -\frac{\Delta}{\gamma}\frac{1}{(r_a + r_s)^2},$$

$$\frac{\partial c}{\partial \alpha} = \lambda_o^{'} S_{in},$$

$$\frac{\partial c}{\partial r_a} = \frac{\partial c}{\partial r_s} = -\lambda_o^{'}\rho L_v\left(q_a^*(T_a) - q_a\right)\frac{1}{(r_a + r_s)^2}.$$

For the second-order (e.g., $\frac{\partial {T_s}^2}{\partial^2 a}$) and degree-2 cross-order (e.g., $\frac{\partial {T_s}^2}{\partial \alpha \partial r_a}$) derivatives, we use MATLAB function "diff" (https://www.mathworks.com/help/matlab/ref/diff.html) to obtain their analytical forms, given the analytical form of LST from FOTSE LST model (Equation 7) or SOTSE LST model (Equation 11). Their expressions are not shown here due to their complexity but can be retrieved from our script posted on GitHub (https://github.com/yaoganchenchi/TRM_Taylor_Series_Expansion/).

It should be pointed out that in our study, all derivatives in Taylor series expansion are evaluated at the reference point (e.g., at T_a for Equations 5 and 6), which follows strictly Taylor's theorem. Similarly, Equations 14 to 19 are computed at the reference state (i.e., before perturbations like $\Delta\alpha$, Δr_a, and Δr_s are applied). However, in practice, the point at which these derivatives are evaluated can be adjusted. For example, there is a long history of evaluating the derivative of Equation 6 at $(T_s + T_a)/2$ in the study of evaporation (Garratt, 1994). In terms of LST attribution, previous studies also introduced empirical ways of adjusting the derivatives computed by Equations 14 to 19 (Liao et al., 2018). We will not study these empirical approaches here but rather evaluate the limitations of FOTSE when it is applied strictly.

2.7. Reanalysis Data

We use Modern-Era Retrospective analysis for Research and Applications, Version 2 (MERRA-2, 0.625° × 0.5°, 1982–2017, monthly) to provide the input or intermediate variables for the TRM method. MERRA-2 is the latest version of reanalysis data produced by NASA's Global Modeling and Assimilation Office, which considers the fully coupled effects and feedbacks between lands, atmosphere, and oceans, as well as assimilates actual observational data (Gelaro et al., 2017). The variables used in this study include air density (ρ), air temperature (T_a), and atmospheric pressure (P) of the lowest atmospheric model layer which is treated as above the blending height, albedo (α), surface emissivity (ε), evapotranspiration (ET), incoming shortwave (S_{in}) and the longwave radiation (L_{in}), outgoing longwave radiation (L_{out}), sensible (H) and latent heat fluxes (LE), and surface exchange coefficient for heat and moisture (C_d). The data analyzed in this study is the climatology from 1982 to 2017 at the annual scale. We calculate the ground heat flux (G) as the residual of the SEB equation, which closes the energy balance. However, since all analyses are carried out at the annual scale, the ground heat flux is small and simply neglected (Purdy et al., 2016).

For the three biophysical factors of interest: albedo (α) is directly provided by MERRA-2; aerodynamic resistance (r_a) is calculated as

Table 1
Mean of Biophysical Factors for Values Located in Their Interquartile Range Based on MERRA-2 Data From 1982 to 2017

Class	α (unitless) (mean ± std.)	r_a (s m^{-1})	r_s (s m^{-1})
Broadleaf/Mixed Forests	0.16 ± 0.03	22 ± 3	83 ± 33
Needleleaf Forests	0.27 ± 0.02	27 ± 5	120 ± 82
Savannas	0.16 ± 0.01	57 ± 9	649 ± 318
Shrublands	0.28 ± 0.05	73 ± 10	1,379 ± 825
Grasslands	0.23 ± 0.03	69 ± 7	409 ± 216
Croplands	0.19 ± 0.02	64 ± 5	269 ± 133
Barren and Urban	0.33 ± 0.04	92 ± 5	60,826 ± 40,461

$$r_a = \frac{\rho}{C_d}, \tag{20}$$

where C_d is the surface exchange coefficient for heat and moisture (kg m^{-2} s^{-1}); surface resistance (r_s) is calculated as

$$r_s = \frac{\rho}{ET\left(q_s^*(T_s) - q_a\right)} - r_a, \tag{21}$$

where ET is the evapotranspiration (kg). Table 1 shows the spatially averaged biophysical factors from their interquartile range (excluding the maximum and minimum 25%) based on MERRA-2 data. The land cover classes are aggregated from the multi-year (2000–2012) mode class of the International Geosphere-Biosphere Programme layer provided by Collection 5 Moderate Resolution Imaging Spectroradiometer land cover products (Friedl et al., 2002) (Figure 1). In Table 1, "Broadleaf Forests" include deciduous broadleaf forests, evergreen broadleaf forests, and mixed forests; "Needleleaf Forests" include deciduous needleleaf forests and evergreen needleleaf forests; "Savannas" include woody savannas and savannas; "Shrublands" include closed shrublands and open shrublands; "Grasslands" include grasslands and cropland/natural vegetation mosaics; "Croplands" only include croplands; "Barren and Urban" includes barren and urban and built-up lands. Due to the spatial averaging, the contrasts among different land cover classes shown in Table 1 include the effects from the differences in surface properties and also from the shifts in climate regimes as well as MERRA-2's uncertainties (Draper et al., 2018). As a result, when performing sensitivity analyses, we will not use the exact values shown in Table 1 but rather treat them as the general guidelines.

We should highlight that the MERRA-2 data are not used to validate the TRM model but to generate a reasonable background climate state as the reference (i.e., before perturbation), based upon which the perturbations are imposed uniformly. In essence, the MERRA-2 data provide the needed forcing data for the TRM model. These forcing data are used to compute the T_s and also examine the ΔT_s in response to the imposed perturbations. To ensure our findings are not dependent on the MERRA-2 data, we also use a different forcing dataset (outputs from the Community Earth System Model or CESM) to drive the TRM model, with the results shown in the supporting information.

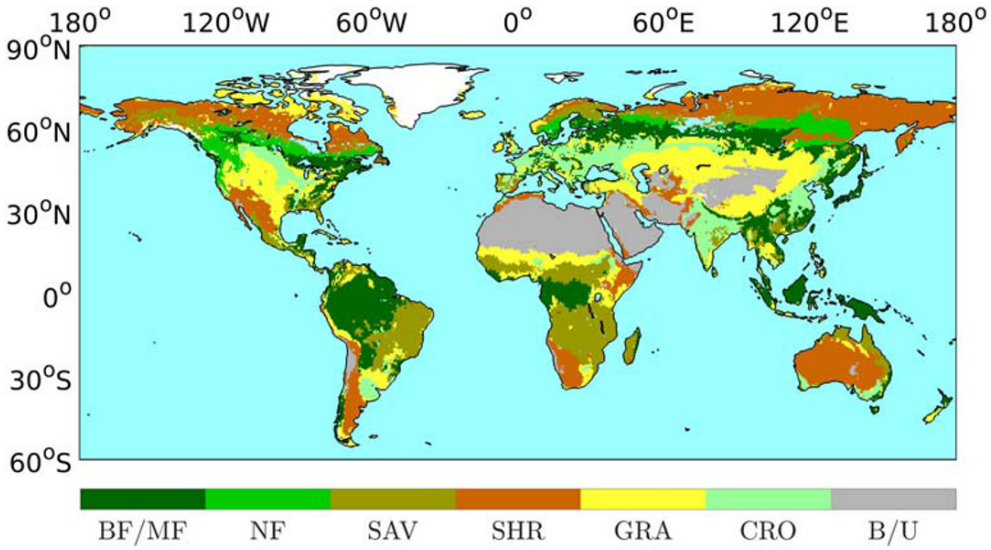

Figure 1. The spatial pattern of the land cover types shown in Table 1. This map is derived from MODIS Collection 5 data. BF/MF is broadleaf and mixed forests, NF is needleleaf forests, SAV is savannas, SHR is shrublands, GRA is grasslands, CRO is croplands, B/U is barren and urban. Cyan depicts water including wetlands, and white depicts snow and ice.

Table 2
List of Symbols for Temperatures

Index	Symbol	Description
a	T_s^{1st} T_s^{2nd}	The superscript over T_s (e.g., T_s^{1st} and T_s^{2nd}) represents the order of Taylor series expansion that is used to obtain the analytical solution of LST, that is, FOTSE LST model (Equation 7) and SOTSE LST model (Equation 11).
b	T_s^{true}	T_s^{true} is treated as the best approximation of the true value of LST. Using Newton's method for the SEB equation (Equation 4), we can iteratively solve the true LST for a given climate forcing (e.g., provided by MERRA-2). The iteration stops when the residual of SEB equation is smaller than 0.0001 W m^{-2}, or the number of iterations reaches 50, either comes first. Note that the LST provided by MERRA-2 cannot be used and is unlikely to be consistent with the T_s^{true} because MERRA-2 uses a complex land surface model, while the LST here is solved by a big-leaf-like one-layer model (Equation 4).
c	ΔT_s^{1st} ΔT_s^{2nd} ΔT_s^{true}	The Greek letter "Δ" means a change. If there is no superscript over Δ, it means the change is directly computed from the analytical solution of LST (e.g., $\Delta T_s^{1st} = T_s^{1st}$ [post perturbation] $- T_s^{1st}$ [before perturbation]). For the before-perturbation case, the annual climatology of MERRA-2 data is used to estimate the temperatures. For the after-perturbation case, we impose perturbations $\Delta\alpha$, Δr_a, and Δr_s on the annual climatology of MERRA-2 data and then estimate the temperatures.
d	$\Delta^{1st}T_s^{1st}$ $\Delta^{1st}T_s^{2nd}$	$\Delta^{1st}T_s^{1st}$ and $\Delta^{1st}T_s^{2nd}$ are changes of LST due to perturbations in biophysical factors estimated by the FOTSE attribution model, that is, Equation 12. This is noted by the superscript "1st" over "Δ." The difference between the two is that they use a different LST model for T_s. The former uses Equation 7 (FOTSE LST model), and the latter uses Equation 11 (SOTSE LST model). This is distinguished by the superscript over T_s.
e	$\Delta^{2nd}T_s^{1st}$ $\Delta^{2nd}T_s^{2nd}$	Similar to d, $\Delta^{2nd}T_s^{1st}$ and $\Delta^{2nd}T_s^{2nd}$ are changes of LST estimated by the SOTSE attribution model, that is, Equation 13. This is distinguished by the superscript "2nd" over "Δ."

2.8. List of Symbols for Temperatures

In this study, there are several T_s and ΔT_s that need to be distinguished. To facilitate our discussion, their definitions are listed in detail in Table 2.

3. Results and Discussion

3.1. Linear Versus Quadratic Approximations of LST

Figures 2a and 2b show the differences between T_s^{1st} and T_s^{true} and between T_s^{2nd} and T_s^{true}, respectively. These biases are introduced by the application of FOTSE and SOTSE to the SEB equation, respectively. As a reference, the spatial pattern of T_s^{true} at the annual scale is shown in Figure 2c. Compared to T_s^{true} obtained with Newton's method, the LST solved by the quadratic equation (i.e., T_s^{2nd}) is more accurate than the LST solved by the linear equation (i.e., T_s^{1st}). In terms of the absolute values, the biases of T_s^{1st} are on the order of 10^{-2} K; the biases of T_s^{2nd} are on the order of 10^{-3} K. In terms of the relative values, the majority of the biases of T_s^{1st} are 10 to 1,000 times larger than the biases of T_s^{2nd} (Figure 3c). The most significant differences between T_s^{2nd} and T_s^{1st} lie in regions such as the tropical evergreen forests, the east coast of the United States, western Canada, and northern Eurasia (Figure 3c). For the signs of the biases, Figure 2a shows that T_s^{1st} always overestimates the true LST. While Figure 2b shows that T_s^{2nd} mostly overestimates the LST, it also underestimates LST over some regions in tropical forests and boreal forests (areas with light blue in Figure 2b, including the Amazon, Indonesia, and western Canada).

In addition, the biases of T_s^{1st} or T_s^{2nd} show clear spatial variabilities across the globe, which are the largest in semi-arid and mountainous areas, such as the western United States, the west coast of South America, sub-Saharan Africa (excluding the rainforests), the India Peninsula, the Qinghai-Tibet Plateau, and Australia (Figures 2a and 2b). Further analysis verifies that their spatial patterns are determined by the difference between the land surface temperature (i.e., T_s^{true}) and the air temperature (i.e., T_a) (Figure 3a). That is to say, the biases in T_s^{1st} or T_s^{2nd} increase as the difference between T_s^{true} and T_a increases, which is reflected in Figure 3b at the annual scale. Mathematically, this is expected because the Taylor series expansion is conducted at the reference point T_a, which also agrees with results from Paw U and Gao (1988). When the difference between T_s^{true} and T_a is smaller than 1 K, the biases in T_s^{1st} or T_s^{2nd} are both small (biases are less than 0.01 K). However, the biases of T_s^{1st} increase much faster than that of T_s^{2nd} when the difference between T_s^{true} and T_a exceeds 1 K.

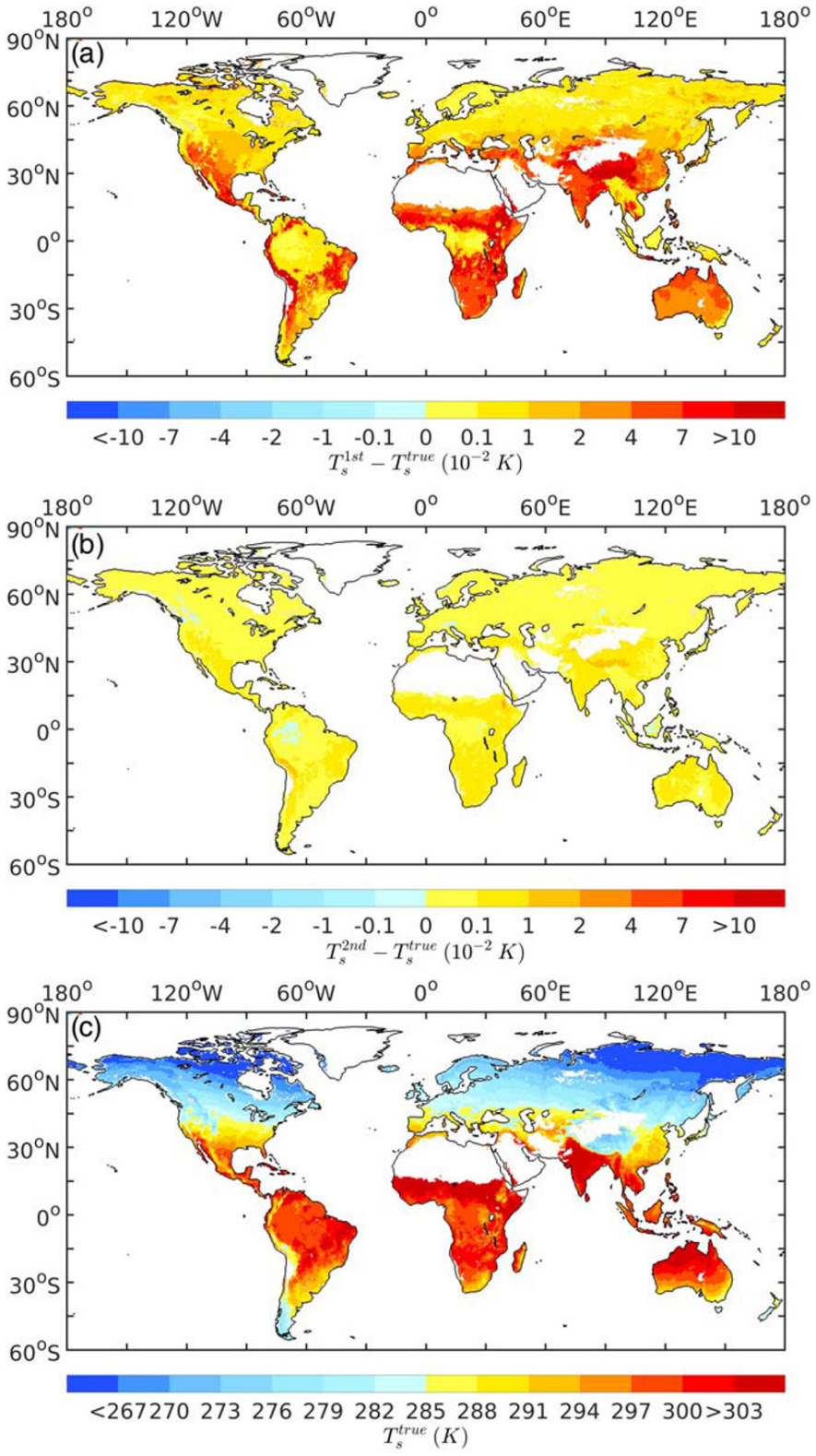

Figure 2. Spatial patterns of the differences (a) between T_s^{1st} and T_s^{true}, and (b) between T_s^{2nd} and T_s^{true}, where T_s^{1st} and T_s^{2nd} are calculated by FOTSE and SOTSE to non-linear terms in the SEB equation, respectively. (c) Map of T_s^{true} calculated by Newton-Raphson iteration. All inputs are the annual climatology of MERRA-2 data from 1982 to 2017.

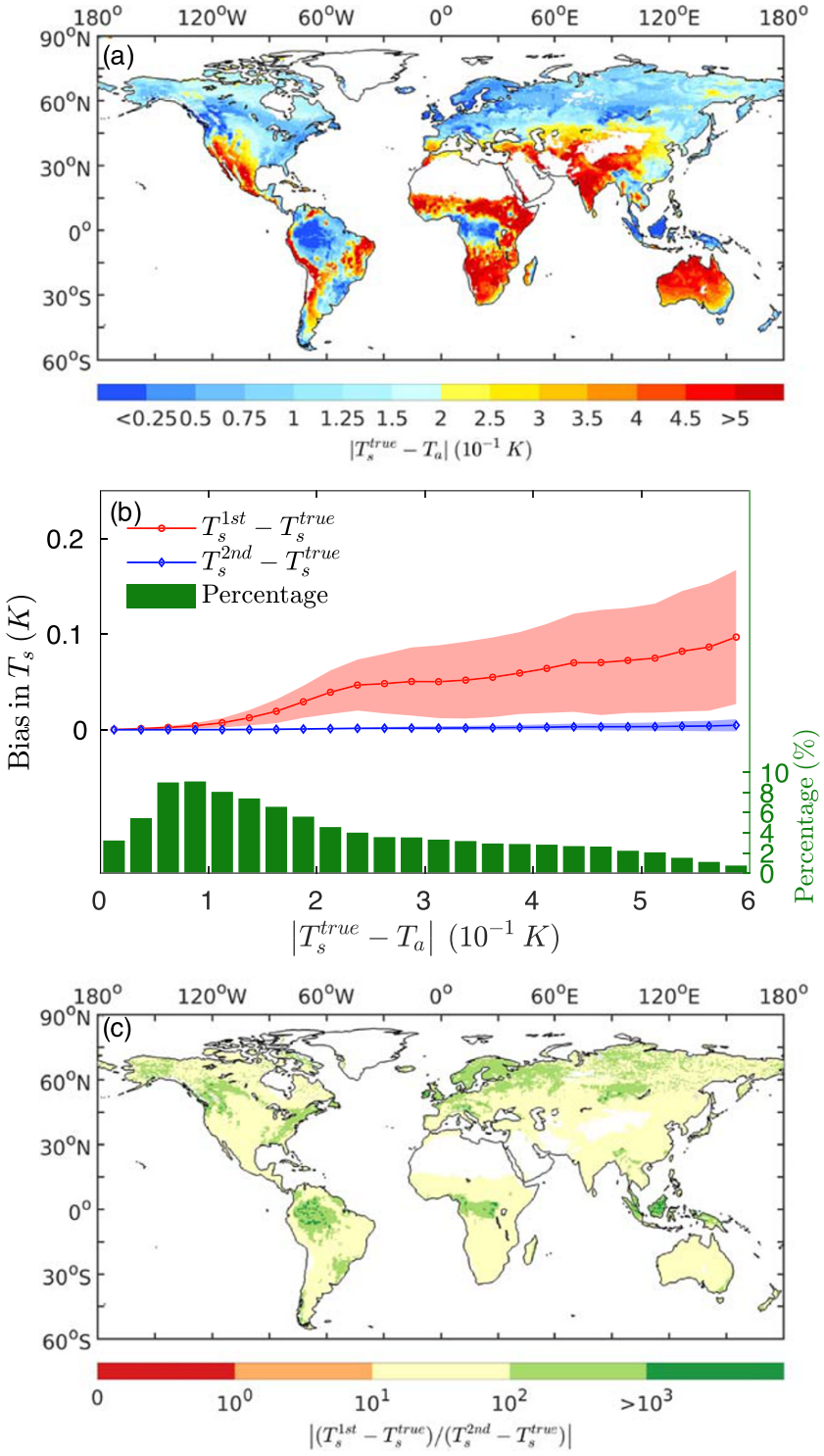

Figure 3. (a) Spatial patterns of the absolute differences between T_s^{true} and T_a. (b) Mean bias between LST (i.e., T_s^{1st} or T_s^{2nd}) and T_s^{true} as a function of the absolute value of difference between T_s^{true} and T_a. The shading area shows one standard deviation of the bias in LST for each bin. (c) Absolute values of the ratio between biases of T_s^{1st} and biases of T_s^{2nd}.

These results are expected mathematically because the use of Taylor series expansion is essentially an approximation to the non-linear terms in the SEB equation, and only a finite number of terms in the approximation are retained. The neglected terms (reflected in the biases) are power functions of the temperature

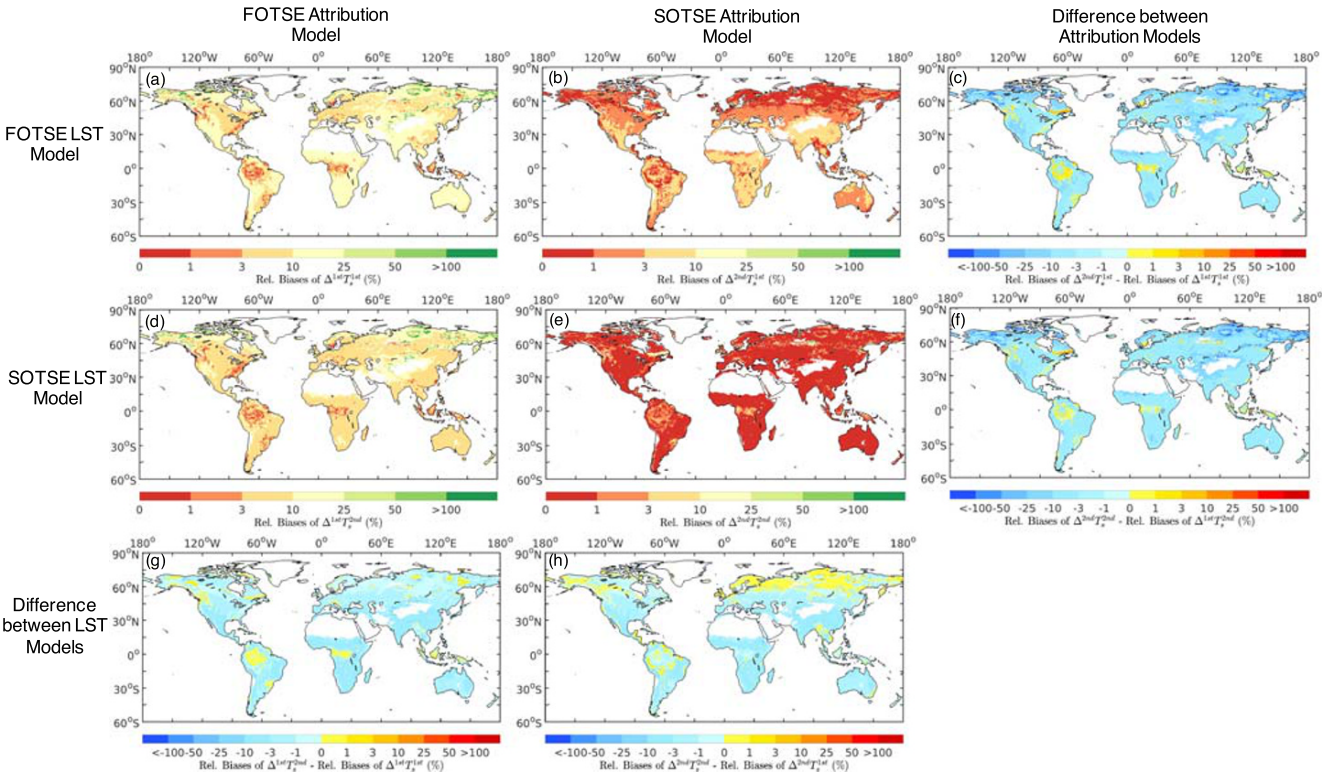

Figure 4. Evaluation of the estimated changes in LST in the small-perturbation case, where $\Delta\alpha = 0.01$, $\Delta r_a = 10$ s m^{-1}, and $\Delta r_s = 10$ s m^{-1}. Spatial patterns of the relative biases of (a) $\Delta^{1st}T_s^{1st}$, (b) $\Delta^{2nd}T_s^{1st}$, (d) $\Delta^{1st}T_s^{2nd}$, and (e) $\Delta^{2nd}T_s^{2nd}$. (c and f) The difference due to attribution models. The difference of the relative biases between (b) and (a) are shown in (c). The difference of the relative biases between (d) and (e) are shown in (f). The contribution from the second-order and cross-order terms is to the opposite of (c) and (f). (g and h) The difference due to the LST models. The difference of the relative biases between (d) and (a) are shown in (g). The difference of the relative biases between (e) and (b) are shown in (h).

difference (i.e., the difference between T_s^{true} and T_a), and they increase more rapidly if the absolute values of temperature difference (i.e., the difference between T_s^{true} and T_a) are higher than 1 K (54% of the vegetated area according to MERRA-2).

3.2. Changes in LST Estimated by FOTSE and SOTSE Attribution Models

The attribution models can reconstruct the changes in LST with given perturbations in each surface biophysical factor (i.e., α, r_a, and r_s). We systematically compare the biases from the LST model and the attribution model. Two experiments with different magnitudes of perturbations are performed, and their results are presented in Figures 4 and 5, respectively. One experiment is conducted with small perturbations in which $\Delta\alpha = 0.01$, $\Delta r_a = 10$ s m^{-1}, and $\Delta r_s = 10$ s m^{-1} (assuming all other input variables for solving T_s^{true} unchanged). The other experiment is performed with large perturbations in which $\Delta\alpha = 0.05$, $\Delta r_a = 50$ s m^{-1}, and $\Delta r_s = 50$ s m^{-1}. As examples, the previously mentioned "Earth greening" (Chen et al., 2019) causes perturbations on the order of $\Delta\alpha = 0.0001$, $\Delta r_a = 2$ s m^{-1}, and $\Delta r_s = 10$ s m^{-1}. On the other hand, deforestation and urbanization can cause perturbations on the order of $\Delta\alpha = 0.1$, $\Delta r_a = 50$ s m^{-1}, and $\Delta r_s = 50$ to 1,000 s m^{-1} and sometimes over tens of thousands of s m^{-1} (Table 1) (Liao et al., 2018). In each experiment, we calculate the biases of the estimated changes in LST from every combination of the LST model and the attribution model with different orders of Taylor series expansion. The biases are normalized by their ΔT_s^{true} per pixel computed by Newton's iterative method.

In the following sections (3.2.1 to 3.2.4), we address four questions:

1. What is the magnitude of the biases in the estimated changes in LST with different models and perturbations?
2. Does the use of FOTSE or SOTSE LST models significantly affect the attribution of changes in LST?

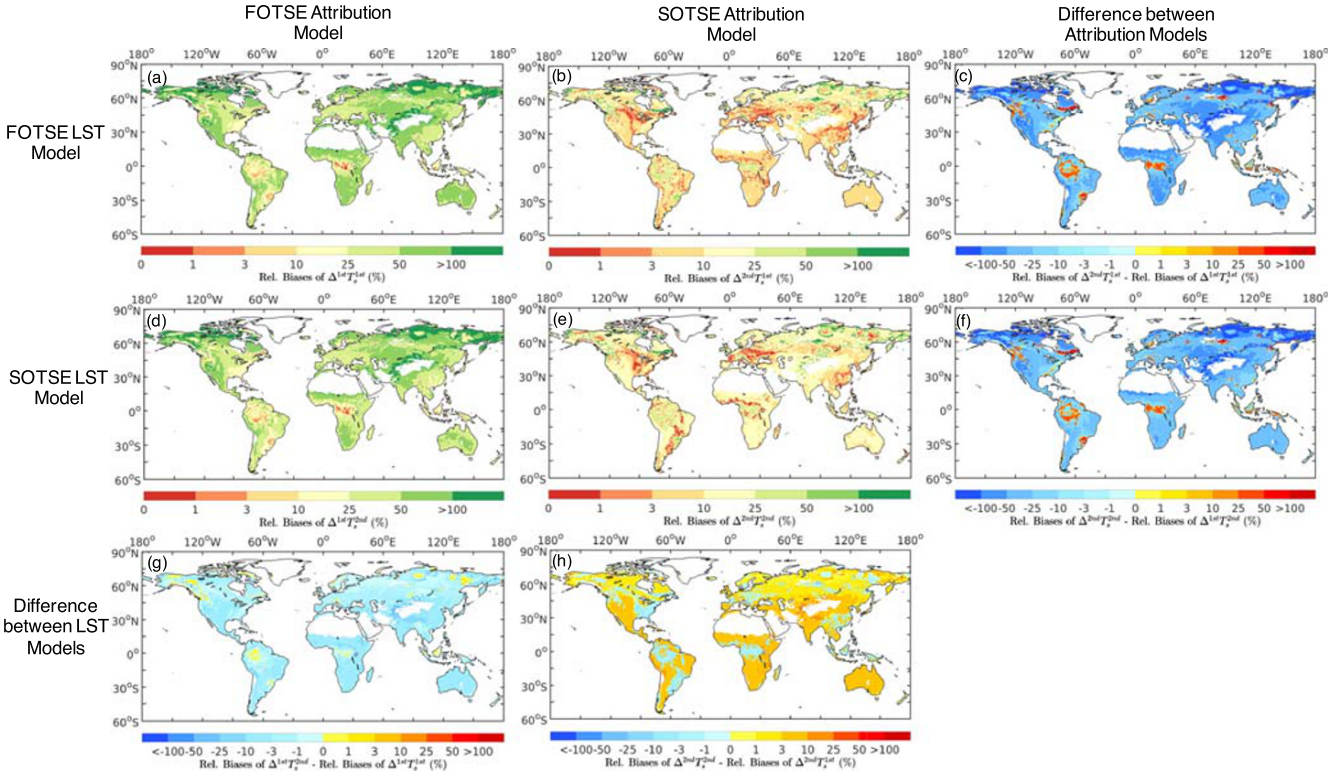

Figure 5. Evaluation of the estimated in changes in LST in the large-perturbation case, where $\Delta\alpha = 0.05$, $\Delta r_a = 50$ s m^{-1}, and $\Delta r_s = 50$ s m^{-1}. Spatial patterns of the relative biases of (a) $\Delta^{1st}T_s^{1st}$, (b) $\Delta^{2nd}T_s^{1st}$, (d) $\Delta^{1st}T_s^{2nd}$, and (e) $\Delta^{2nd}T_s^{2nd}$. (c and f) The difference due to attribution models. The difference of the relative biases between (b) and (a) are shown in (c). The difference of the relative biases between (d) and (e) are shown in (f). The contribution from the second-order and cross-order terms is to the opposite of (c) and (f). (g and h) The difference due to the LST models. The difference of the relative biases between (d) and (a) are shown in (g). The difference of the relative biases between (e) and (b) are shown in (h).

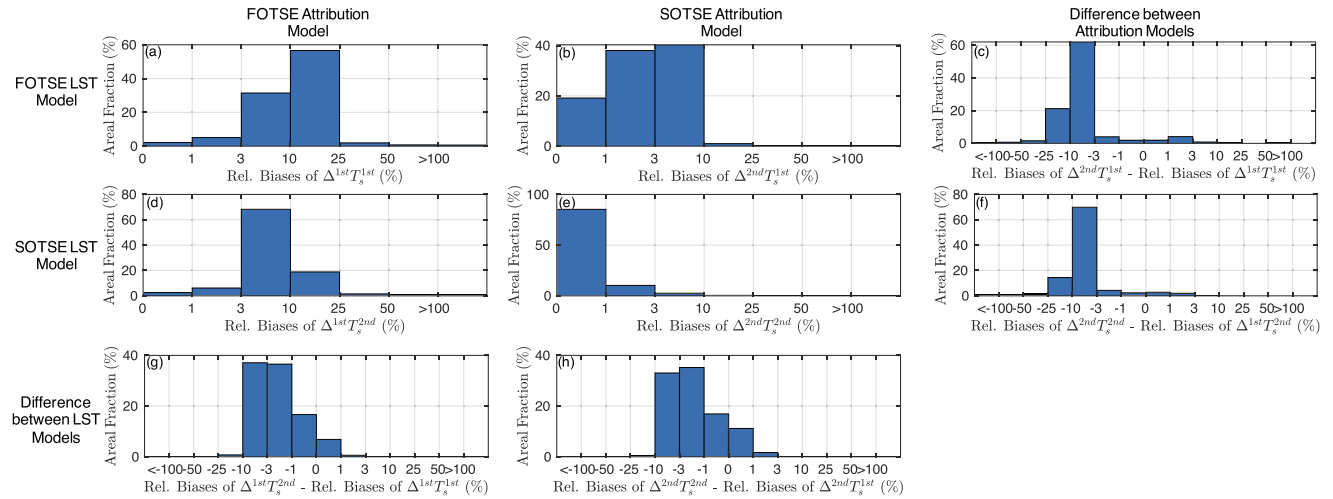

Figure 6. Histograms of the relative biases in changes in LST in the small-perturbation case, where $\Delta\alpha = 0.01$, $\Delta r_a = 10$ s m^{-1}, and $\Delta r_s = 10$ s m^{-1}. This figure corresponds to Figure 3. Histograms of the relative biases for (a) $\Delta^{1st}T_s^{1st}$, (b) $\Delta^{2nd}T_s^{1st}$, (d) $\Delta^{1st}T_s^{2nd}$, and (e) $\Delta^{2nd}T_s^{2nd}$. (c and f) The difference due to attribution models. The difference of the relative biases between (b) and (a) are shown in (c). The difference of the relative biases between (d) and (e) are shown in (f). (g and h) The difference due to the LST models. The difference of the relative biases between (d) and (a) are shown in (g). The difference of the relative biases between (e) and (b) are shown in (h).

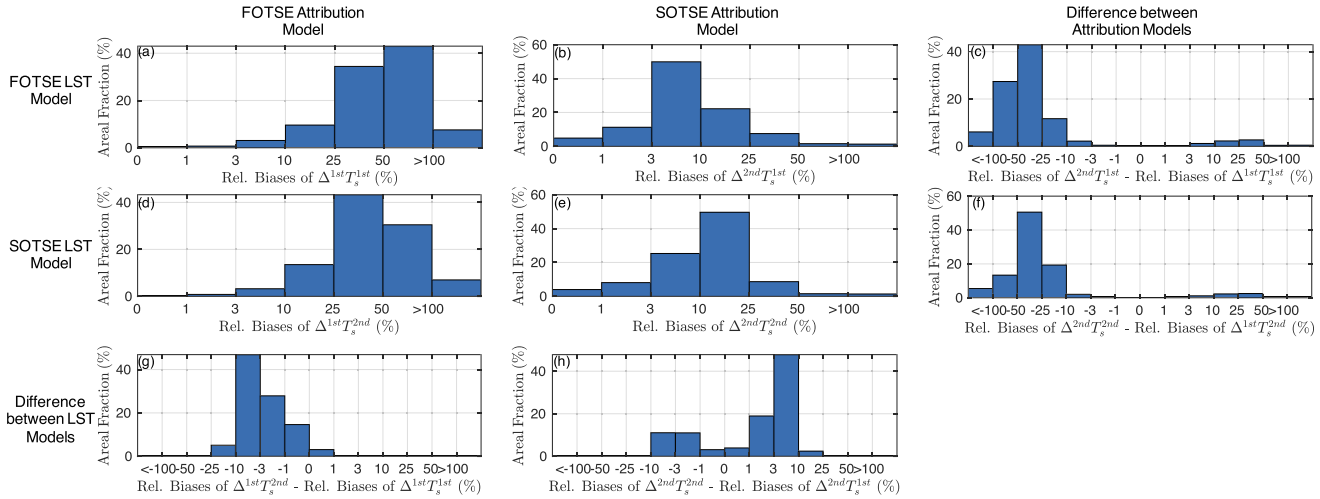

Figure 7. Histograms of the relative biases in changes in LST in the large-perturbation case, where $\Delta\alpha = 0.05$, $\Delta r_a = 50$ s m^{-1}, and $\Delta r_s = 50$ s m^{-1}. This figure corresponds to Figure 4. Histograms of the relative biases for (a) $\Delta^{1st}T_s^{1st}$, (b) $\Delta^{2nd}T_s^{1st}$, (d) $\Delta^{1st}T_s^{2nd}$, and (e) $\Delta^{2nd}T_s^{2nd}$. (c and f) The difference due to attribution models. The difference of the relative biases between (b) and (a) are shown in (c). The difference of the relative biases between (d) and (e) are shown in (f). (g and h) The difference due to the LST models. The difference of the relative biases between (d) and (a) are shown in (g). The difference of the relative biases between (e) and (b) are shown in (h).

3. What is the role of the order of Taylor series expansion in the attribution model in estimating the changes in LST?
4. How are individual contribution terms changed or improved by using a higher-order model?

3.2.1. The Magnitude of Biases

Panels a, b, d, and e in Figures 4 and 5 show the spatial patterns of the relative biases of $\Delta^{1st}T_s^{1st}$, $\Delta^{2nd}T_s^{1st}$, $\Delta^{1st}T_s^{2nd}$, and $\Delta^{2nd}T_s^{2nd}$, which represent different combinations of the LST models and attribution models (see Table 2). Similar results but with the CESM forcing instead of MERRA-2 are shown in the supporting information. In addition, Figures 6 and 7 show histograms of the relative biases of the estimated changes in LST, which complement Figures 4 and 5, respectively.

For the small-perturbation case (Figures 4a, 4b, 4d, and 4e), we find that biases become smaller as the order of Taylor series expansion increases in the LST model and the attribution model at the global scale: The biases are the largest in the approach with the FOTSE LST model and FOTSE attribution model (i.e., $\Delta^{1st}T_s^{1st}$ in Figure 4a), most of which are located in the 10–25% category (Figure 6a). The biases are the smallest in the approach with the SOTSE LST model and SOTSE attribution model (i.e., $\Delta^{2nd}T_s^{2nd}$; Figure 4e), most of which are on the order of 1% (Figure 6d).

For the large-perturbation case (Figure 5), we find that biases decrease when the order of Taylor series expansion increases in the attribution model, but they do not consistently decrease as the order of Taylor series expansion increases in the LST model. Similar to the small-perturbation case, the largest biases are observed in $\Delta^{1st}T_s^{1st}$, which is around 50% on average (Figures 5a and 7a). However, $\Delta^{2nd}T_s^{1st}$ (Figure 5b), instead of $\Delta^{2nd}T_s^{2nd}$, has the smallest biases, and most of them are located in the 3–10% category (Figure 7b). In general, the magnitude of biases in the large-perturbation case is larger than its counterpart in the small-perturbation case, which implies that the higher-order and higher-degree cross-order terms may have non-negligible contributions when the perturbations in biophysical factors are large.

3.2.2. The Role of the Order of Taylor Series Expansion for the LST Model

For the small-perturbation case, the first row of Figure 4 uses the LST solved by the linear equation (T_s^{1st}), while the second row employs the LST solved by the quadratic equation (T_s^{2nd}). The comparison between these two rows reveals the difference induced by LST models (Figures 4g and 4h). In general, we find that the relative biases of the changes in LST estimated with T_s^{2nd} could be up to 10% smaller than the biases estimated with T_s^{1st} regardless of the order of the attribution model (Figures 6g and 6h). Nevertheless, we note

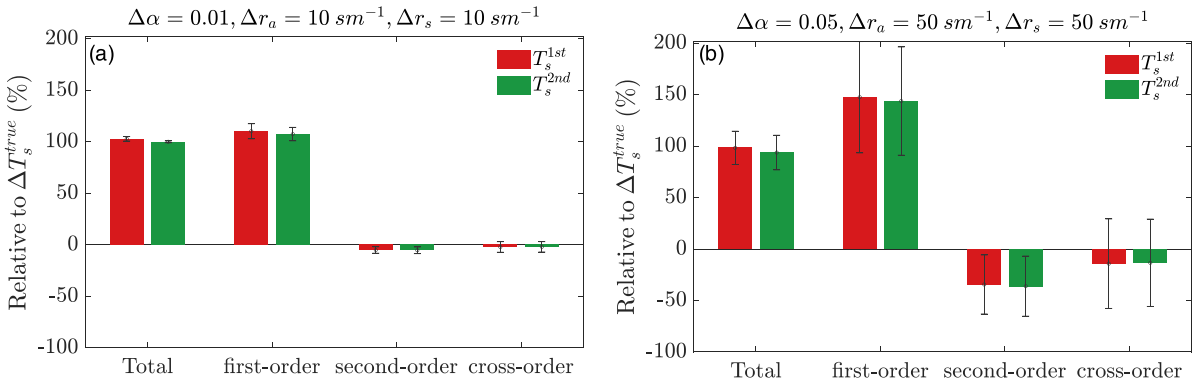

Figure 8. Attribution of changes in LST by terms with different Taylor series expansion orders in the attribution model. (a) Small-perturbation case: $\Delta\alpha = 0.01$, $\Delta r_a = 10$ s m^{-1}, $\Delta r_s = 10$ s m^{-1}. (b) Large-perturbation case: $\Delta\alpha = 0.05$, $\Delta r_a = 50$ s m^{-1}, $\Delta r_s = 50$ s m^{-1}. The data are averaged at the global level excluding the highest and lowest 1%. Total is the sum of the first-order, second-order, and cross-order terms. The red bar is calculated by T_s^{1st}, and the green bar is calculated by T_s^{2nd}. The error bars are one standard deviation of the spatial variability.

that the biases can be slightly larger (about 0–1%) in the attribution model using T_s^{2nd} than that using T_s^{1st} in some regions over tropical and boreal forests (Figures 4g and 4h).

For the large-perturbation case with the FOTSE attribution model, most of the relative biases of the changes in LST estimated with T_s^{2nd} are smaller than those estimated with T_s^{1st} (Figures 5g and 7g). However, for the large-perturbation case with the SOTSE attribution model, most of the relative biases of the changes in LST estimated with T_s^{2nd} are larger than those estimated with T_s^{1st} (Figures 5f and 7f). To summarize, a higher-order LST model does not guarantee lower biases in the changes in LST for large-perturbation cases.

3.2.3. The Role of the Order of Taylor Series Expansion for the Attribution Model

Using the large-perturbation case as an example (Figure 5), the first column (Figures 5a and 5d) shows the relative accuracy of changes in LST computed from the FOTSE attribution model (Equation 12). The second column (Figures 5b and 5e) shows the relative accuracy of changes in LST computed from the SOTSE attribution model (Equation 13). The third column (Figures 5c and 5f) shows the difference between the second column and the first column, which illustrates that, in general, the biases of changes in LST estimated by the SOTSE attribution model are smaller than that by the FOTSE attribution model. In addition, the analysis of the small-perturbation case confirms that the SOTSE attribution model performs better than the FOTSE attribution model given the same LST model (Figure 4). Close inspection shows that the performance improvement from the SOTSE attribution model is more evident in the large-perturbation case than that in the small-perturbation case. Compared to the FOTSE attribution model, the reduction of biases from the SOTSE attribution model ranges from 10% to 100% in the large-perturbations case (Figures 7c and 7f), while in the small-perturbation case, the reduction is 3% to 25% (Figures 6c and 6f). The difference between SOTSE and FOTSE is the contribution from second-order terms and cross-order terms (Figures 4c, 4f, 5c, and 5f). This contribution is strongest in a few regions over tropical and boreal forests and widespread in pan-arctic shrubs and tundra. We note that a few areas in tropical forests and boreal forests are exceptional—where the SOTSE attribution model performs worse (i.e., larger biases) than the FOTSE attribution model (Figures 4c, 4f, 5c, and 5f).

Therefore, the above comparisons through sections 3.2.1 to 3.2.3 indicate that using a SOTSE attribution model improves the accuracy of the estimated changes in LST more effectively than using a SOTSE LST model (T_s^{2nd}) which may even cause adverse effects in a few regions. Our results also suggest that the advantage of the SOTSE attribution model is more evident in a large-perturbation case than in a small-perturbation case.

3.2.4. Component Analysis for SOTSE Attribution Models

To understand why the SOTSE attribution models perform better than the FOTSE ones, we decompose the changes in LST for the small- and large-perturbation cases, respectively, into relative contributions from first-order terms, second-order terms, and degree-2 cross-order terms, and the Total is the sum of the three. In the large-perturbation case (Figure 8b), the first-order terms from the attribution model significantly

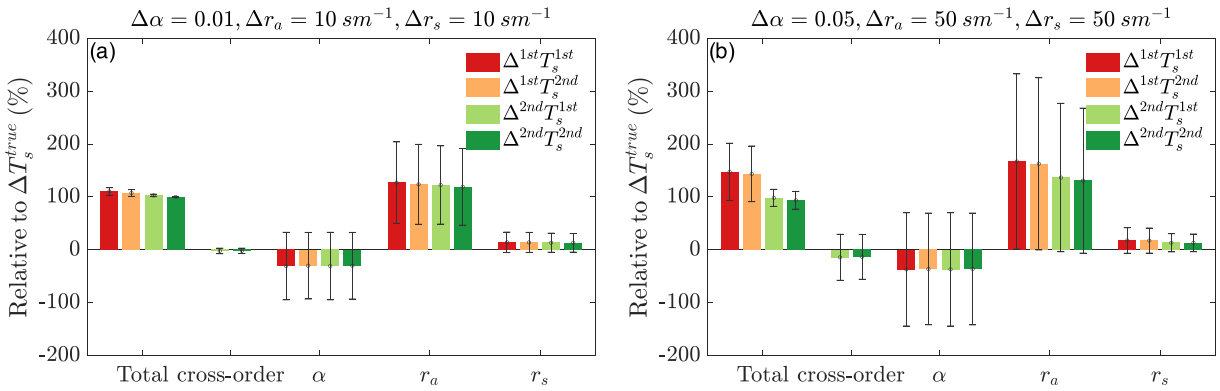

Figure 9. Attribution of changes in LST by biophysical variables. (a) Small-perturbation case: $\Delta\alpha = 0.01$, $\Delta r_a = 10$ s m^{-1}, $\Delta r_s = 10$ s m^{-1}. (b) Large-perturbation case: $\Delta\alpha = 0.05$, $\Delta r_a = 50$ s m^{-1}, $\Delta r_s = 50$ s m^{-1}. The values displayed are the global average excluding the highest and lowest 1%. The color encodes different order of Taylor series expansion for the LST and the attribution models (see Table 2). There are no cross-order terms in the attribution model using T_s^{1st}. The error bars are one standard deviation of the spatial variability.

overestimate the changes in LST by as large as 50% on average. The biases are dramatically reduced after considering the second-order terms and the degree-2 cross order terms because they have an opposite sign compared to the first-order terms. The small-perturbation case (Figure 8a) also reveals similar results as the large-perturbation case, but with a smaller contribution from the second-order terms and the degree-2 cross-order terms.

Similarly, we also decompose the changes in LST into contributions from three biophysical factors (α, r_a, and r_s) and their degree-2 cross-order terms (the sum of every combination of two factors among α, r_a, and r_s). The goal of this analysis is not to compare the relative importance among α, r_a, and r_s. Instead, our goal is to identify which contribution has changed the most among the biophysical factors by adding the second-order terms and the degree-2 cross-order terms in the attribution analysis. In Figure 9, we can see reductions in the contribution from the r_a pathway if the second-order and degree-2 cross-order terms are considered, especially in the large-perturbation case where the magnitude of cross-order terms is almost equally important as that of r_s (Figure 9b). This implies that the independence assumption of the attributable factors may not hold in the large-perturbation case, although it roughly holds in the small-perturbation case.

3.3. Sensitivity Analysis for Individual Perturbations

Previous results suggest that the biases in the estimated changes in LST are a function of the magnitude of the disturbances. Therefore, in this section, we conduct sensitivity analyses for the biases of the estimated changes in LST when only one variable is perturbed. This eliminates the cross-order terms, but the contribution from higher-order terms is retained. Figure 10 shows the absolute values of biases normalized by ΔT_s^{true} and averaged across the globe.

3.3.1. Albedo

For the albedo, the imposed perturbations range from 0.1 to 0.15. This covers the range of albedo change between any two land cover types based on MERRA-2 data (Table 1). The magnitude of the biases within our experimental range is within 2% (relative to ΔT_s^{true}), which are much smaller than the biases induced by the perturbations from aerodynamic resistance and surface resistance. For models using $T_s^{1\text{st}}$, the biases decrease as the perturbation increases (Figure 10a). We note that the biases are identical for experiments with different orders of Taylor series expansion in the attribution model (Figure 10a) when using $T_s^{1\text{st}}$ because the nth ($n > 1$) derivative of $T_s^{1\text{st}}$ to α is zero. For models using $T_s^{2\text{nd}}$ (Figure 10b), the biases of $\Delta^{1\text{st}}T_s^{2\text{nd}}$ are smaller than those of $\Delta^{2\text{nd}}T_s^{2\text{nd}}$ when the perturbation of α is below a critical value around 0.06. Beyond that critical value, $\Delta^{2\text{nd}}T_s^{2\text{nd}}$ performs better than $\Delta^{1\text{st}}T_s^{2\text{nd}}$.

3.3.2. Aerodynamic Resistance

For the aerodynamic resistance, the perturbations range from 10 to 200 s m^{-1}. This also covers the range of aerodynamic resistance change between any two land cover types (Table 1). Figures 10b and 10e show that,

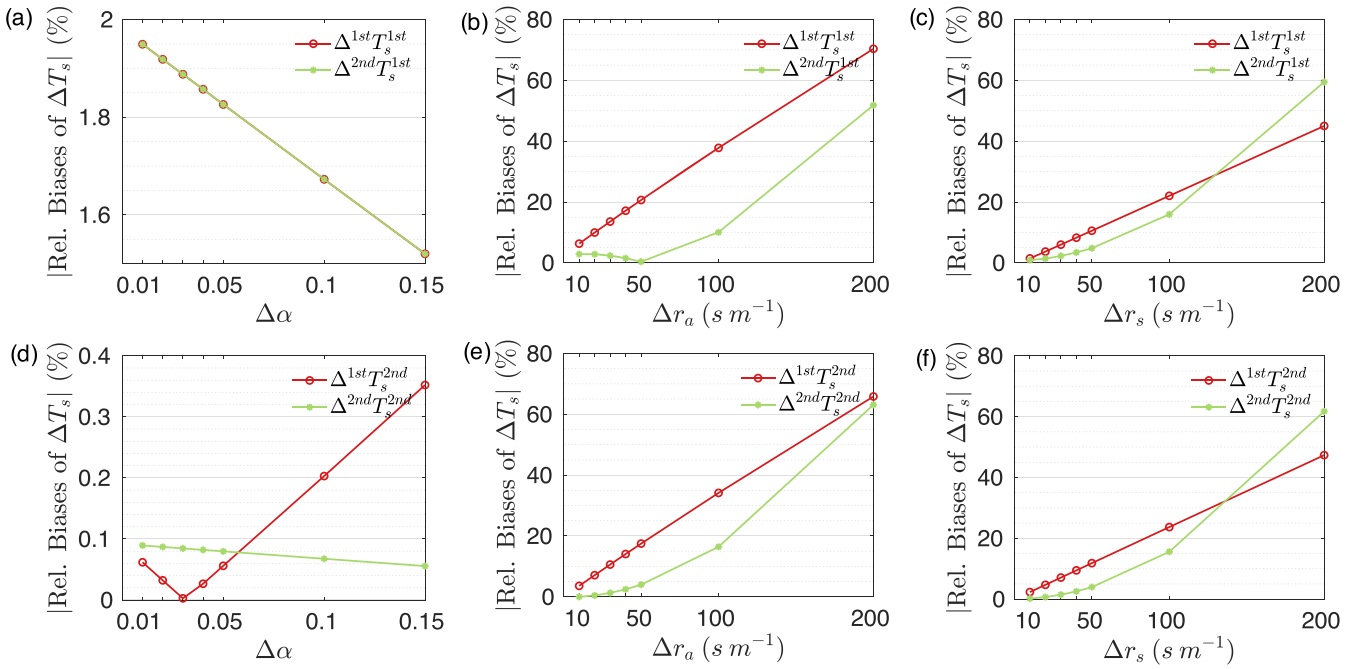

Figure 10. Absolute sensitivity of the relative biases in estimated change in LST by biophysical variable. Sensitivity of mean biases with (a) α perturbations, (b) r_a perturbations, and (c) r_s perturbations based on FOTSE LST model (i.e., T_s^{1st}). Sensitivity of mean biases with (d) α perturbations, (e) r_a perturbations, and (f) r_s perturbations based on SOTSE LST model (i.e., T_s^{2nd}). The values displayed are the global average excluding the highest and lowest 1%.

expect for $\Delta^{2nd}T_s^{1st}$, the biases increase monotonically as the magnitude of perturbation increases. When the perturbation is 10 s m^{-1}, the biases are about 5%. When the perturbation is 50 s m^{-1}, the biases are about 20%. It also reveals that, within our imposed perturbation range and given the same LST model, the SOTSE attribution model performs better than the FOTSE attribution model.

3.3.3. Surface Resistance

For the surface resistance, the range of perturbations is identical to that of aerodynamic resistance, from 10 to 200 s m^{-1}. Figures 10c and 10f show that for any combination of the LST model and the attribution model, the biases increase monotonically as the magnitude of perturbation increases. In general, the biases for surface resistance are of the same order of magnitude as those for aerodynamic resistance (Figure 10). When the perturbation is 10 s m^{-1}, the biases are within 2%. When the perturbation is 50 s m^{-1}, the biases are about 10%. Interestingly, we find that the SOTSE attribution model starts to have larger biases than the FOTSE attribution when the perturbation exceeds a critical value of around 130 s m^{-1}, and this difference seems to become larger as the perturbation further increases. This suggests that the non-linear effects associated with large perturbations in surface resistance are too strong to be captured by SOTSE. An alternative solution to reduce the biases is to consider even higher-order terms in the attribution model (third-order terms, degree-3 cross-order terms, fourth-order terms, and degree-4 cross-order terms). Linking this back to LULCC, changes in surface resistance due to land cover transitions from forests to non-forest classes can be larger than 200 s m^{-1} (Table 1) (Tao et al., 2013; Wilson et al., 2002). Therefore, surface resistance may be a major factor in generating biases in the attribution analysis, especially when the perturbations are large.

4. Conclusions

In this study, we evaluate the biases of using Taylor series expansion to solve LST and estimate its changes due to LULCC-induced biophysical changes. These biases are twofold from (1) the LST model and (2) the attribution model. Our analyses show that the accuracy of the LST model decreases as the discrepancy between LST and air temperature increases. They also indicate that the biases in the SOTSE LST model

are smaller than those of the FOTSE LST model. Nevertheless, the order of Taylor series expansion in the LST model does not significantly influence the attribution of changes in LST.

By analyzing the biases of different orders of Taylor series expansion in the attribution model, we find that the SOTSE attribution model is considerably more accurate than the FOTSE attribution model, and this contrast is more evident when the perturbations are large. In other words, this suggests that contributions from higher-order and cross-order terms neglected by the linearization processes can play an essential role in the attribution model. Therefore, these biophysical factors should not be treated as independent under large perturbations. Sensitivity analysis further shows that non-linear effects associated with changes in surface resistance are particularly strong for LULCC scenarios with large disturbances such as deforestation and urbanization. In conclusion, we recommend using the SOTSE or even higher-order Taylor series expansion attribution models to reduce the biases in the estimated changes in LST. However, the FOTSE LST model suffices and is recommended due to its simplicity.

Lastly, we need to acknowledge that while the SOTSE attribution model improves over the FOTSE model, it does not address other assumptions involved in solving the surface energy balance equation in a simplified way (as in the TRM method and many other methods). Two notable examples include treating ground heat flux as a forcing and the assumption of no atmospheric response to LULCC. The treatment of ground heat flux as a forcing instead of a response has a long history in deriving simplified equations for estimating evaporation (e.g., the Penman and Penman-Monteith equation). The biggest disadvantage of this treatment is that the ground heat flux needs to be known a priori, which is obviously very challenging except at long time scales when the ground heat flux can be assumed to be zero (as in this study). This treatment can be relaxed by using a model for the ground heat flux (see Wang et al., 2020, for an example by using the so-called force-restore method). This is important when the goal was to understand how the ground heat flux, together with LST, also responds to LULCC or when the dynamics of ground heat flux are important for modulating the response of LST to LULCC (e.g., at short time scales).

The assumption of no atmospheric response to LULCC is also important to appreciate. There are two ways of interpreting this assumption. One is that the scale characterizing the perturbations induced by LULCC is so small that the response of atmospheric conditions at the vertical level that provides forcing to the land is minimal. Another way is that the atmospheric forcing is always taken from above the blending height at which the heterogeneity at the surface is mixed up by the integrating power of turbulence. Either way, there is a constraint on the scale characterizing the perturbations induced by LULCC, which depends on the height at which the atmospheric forcing is supplied (Li & Wang, 2019). As the scale of the perturbation increases, it might become impossible for find a vertical level in the atmospheric boundary layer to prescribe the same forcing for both the reference land and the perturbed land. Under such conditions, one should treat the land-atmospheric boundary layer as a coupled system, instead of a decoupled system as the one dealt with here. That is, one should consider the atmospheric response to the perturbations as part of the problem. This can be achieved by using convective boundary layer models or models based on the advection-diffusion equations, as discussed in Li and Wang (2019).

Conflict of Interest

The authors declare no conflicts of interests.

Data Availability Statement

All data analyzed in this study are publicly available as referenced within the article. The script of TRM derivatives (DOI: 10.5281/zenodo.3753088) is available online (https://github.com/yaoganchenchi/TRM_Taylor_Series_Expansion/).

Acknowledgments

This work is supported by the U.S. Army Research Office under Grant W911NF-18-1-0360 and the U.S. National Science Foundation under Grant AGS-1853354. R. B. M acknowledges funding from NASA Earth Science Division.

References

Alkama, R., & Cescatti, A. (2016). Biophysical climate impacts of recent changes in global forest cover. *Science*, *351*(6273), 600–604. https://doi.org/10.1126/science.aac8083

Bonan, G. B. (2008). Forests and climate change: Forcings, feedbacks, and the climate benefits of forests. *Science*, *320*(5882), 1444–1449. https://doi.org/10.1126/science.1155121

Bright, R. M., Davin, E., O'Halloran, T., Pongratz, J., Zhao, K., & Cescatti, A. (2017). Local temperature response to land cover and management change driven by non-radiative processes. *Nature Climate Change*, *7*(4), 296–302. https://doi.org/10.1038/nclimate3250

Brutsaert, W. (2005). *Hydrology*. Cambridge: Cambridge University Press.
Brutsaert, W. (2013). *Evaporation into the atmosphere*. Dordrecht: Springer Science & Business Media.
Burakowski, E., Tawfik, A., Ouimette, A., Lepine, L., Novick, K., Ollinger, S., et al. (2018). The role of surface roughness, albedo, and Bowen ratio on ecosystem energy balance in the eastern United States. *Agricultural and Forest Meteorology*, *249*, 367–376. https://doi.org/10.1016/j.agrformet.2017.11.030
Chen, C., Park, T., Wang, X., Piao, S., Xu, B., Chaturvedi, R. K., et al. (2019). China and India lead in greening of the world through land-use management. *Nature Sustainability*, *2*(2), 122–129. https://doi.org/10.1038/s41893-019-0220-7
Chen, L., & Dirmeyer, P. A. (2016). Adapting observationally based metrics of biogeophysical feedbacks from land cover/land use change to climate modeling. *Environmental Research Letters*, *11*(3), 034002. https://doi.org/10.1088/1748-9326/11/3/034002, 034002
Devaraju, N., de Noblet-Ducoudré, N., Quesada, B., & Bala, G. (2018). Quantifying the relative importance of direct and indirect biophysical effects of deforestation on surface temperature and teleconnections. *Journal of Climate*, *31*(10), 3811–3829. https://doi.org/10.1175/JCLI-D-17-0563.1
Dingman, S. L. (2008). *Physical hydrology*. Long Grove: Waveland Press Inc.
Draper, C. S., Reichle, R. H., & Koster, R. D. (2018). Assessment of MERRA-2 land surface energy flux estimates. *Journal of Climate*, *31*(2), 671–691. https://doi.org/10.1175/JCLI-D-17-0121.1
Duveiller, G., Hooker, J., & Cescatti, A. (2018). The mark of vegetation change on Earth's surface energy balance. *Nature Communications*, *9*(1), 679. https://doi.org/10.1038/s41467-017-02810-8
Friedl, M. A., McIver, D. K., Hodges, J., & Zhang, X. Y. (2002). Global land cover mapping from MODIS: Algorithms and early results. *Remote Sensing of Environment*, *83*(1–2), 287–302. https://doi.org/10.1016/s0034-4257(02)00078-0
Garratt, J. R. (1994). *The atmospheric boundary layer*. Cambridge: Cambridge University Press.
Ge, J., Guo, W., Pitman, A. J., De Kauwe, M. G., Chen, X., & Fu, C. (2019). The nonradiative effect dominates local surface temperature change caused by afforestation in China. *Journal of Climate*, *32*(14), 4445–4471. https://doi.org/10.1175/JCLI-D-18-0772.1
Gelaro, R., McCarty, W., Suarez, M. J., Todling, R., Molod, A., Takacs, L., et al. (2017). The Modern-Era Retrospective Analysis for Research and Applications, Version 2 (MERRA-2). *Journal of Climate*, *30*(14), 5419–5454. https://doi.org/10.1175/JCLI-D-16-0758.1
Juang, J.-Y., Katul, G., Siqueira, M., Stoy, P., & Novick, K. (2007). Separating the effects of albedo from eco-physiological changes on surface temperature along a successional chronosequence in the southeastern United States. *Geophysical Research Letters*, *34*. https://doi.org/10.1029/2007GL031296
Keenan, T. F., Prentice, I. C., Canadell, J. G., Williams, C. A., Wang, H., Raupach, M., & Collatz, G. J. (2016). Recent pause in the growth rate of atmospheric CO_2 due to enhanced terrestrial carbon uptake. *Nature Communications*, *7*(1), 13428. https://doi.org/10.1038/ncomms13428
Lee, X., Goulden, M. L., Hollinger, D. Y., Barr, A., Black, T. A., Bohrer, G., et al. (2011). Observed increase in local cooling effect of deforestation at higher latitudes. *Nature*, *479*(7373), 384–387. https://doi.org/10.1038/nature10588
Li, D., & Bou-Zeid, E. (2013). Synergistic interactions between urban heat islands and heat waves: The impact in cities is larger than the sum of its parts. *Journal of Applied Meteorology and Climatology*, *52*(9), 2051–2064. https://doi.org/10.1175/JAMC-D-13-02.s1
Li, D., Liao, W., Rigden, A. J., Liu, X., Wang, D., Malyshev, S., & Shevliakova, E. (2019). Urban heat island: Aerodynamics or imperviousness? *Science Advances*, *5*(4). https://doi.org/10.1126/sciadv.aau4299
Li, D., & Wang, L. (2019). Sensitivity of surface temperature to land use and land cover change-induced biophysical changes: The scale issue. *Geophysical Research Letters*, *46*, 9678–9689. https://doi.org/10.1029/2019GL084861
Li, Y., Guan, K., Peng, B., Franz, T. E., Wardlow, B., & Pan, M. (2020). Quantifying irrigation cooling benefits to maize yield in the US Midwest. *Global Change Biology*, *2216*(1), 3065–3078. https://doi.org/10.1111/gcb.15002
Liao, W., Rigden, A. J., & Li, D. (2018). Attribution of local temperature response to deforestation. *Journal of Geophysical Research: Biogeosciences*, *123*, 1572–1587. https://doi.org/10.1029/2018JG004401
Luyssaert, S., Jammet, M., Stoy, P. C., Estel, S., Pongratz, J., Ceschia, E., et al. (2014). Land management and land-cover change have impacts of similar magnitude on surface temperature. *Nature Climate Change*, *4*(5), 389–393. https://doi.org/10.1038/nclimate2196
Mahmood, R., Pielke, R. A. Sr., Hubbard, K. G., Niyogi, D., Dirmeyer, P. A., McAlpine, C., et al. (2013). Land cover changes and their biogeophysical effects on climate. *International Journal of Climatology*, *34*(4), 929–953. https://doi.org/10.1002/joc.3736
Monteith, J., & Unsworth, M. (2007). *Principles of environmental physics*. Amsterdam: Academic Press.
Moon, M., Li, D., Liao, W., Rigden, A. J., & Friedl, M. A. (2020). Modification of surface energy balance during springtime: The relative importance of biophysical and meteorological changes. *Agricultural and Forest Meteorology*, *284*, 107905. https://doi.org/10.1016/j.agrformet.2020.107905
Paw U, K. T., & Gao, W. (1988). Applications of solutions to non-linear energy budget equations. *Agricultural and Forest Meteorology*, *43*(2), 121–145. https://doi.org/10.1016/0168-1923(88)90087-1
Pielke, R. A. Sr., Pitman, A., Niyogi, D., Mahmood, R., McAlpine, C., Hossain, F., et al. (2011). Land use/land cover changes and climate: Modeling analysis and observational evidence. *Wiley Interdisciplinary Reviews: Climate Change*, *2*(6), 828–850. https://doi.org/10.1002/wcc.144
Purdy, A. J., Fisher, J. B., Goulden, M. L., & Famiglietti, J. S. (2016). Ground heat flux: An analytical review of 6 models evaluated at 88 sites and globally. *Journal of Geophysical Research: Biogeosciences*, *121*, 3045–3059. https://doi.org/10.1002/2016JG003591
Rigden, A. J., & Li, D. (2017). Attribution of surface temperature anomalies induced by land use and land cover changes. *Geophysical Research Letters*, *44*, 6814–6822. https://doi.org/10.1002/2017GL073811
Roderick, M. L., Rotstayn, L. D., Farquhar, G. D., & Hobbins, M. T. (2007). On the attribution of changing pan evaporation. *Geophysical Research Letters*, *34*, 35, L17403–36. https://doi.org/10.1029/2007GL031166
Tao, Z., Santanello, J. A., Chin, M., Zhou, S., Tan, Q., Kemp, E. M., & Peters-Lidard, C. D. (2013). Effect of land cover on atmospheric processes and air quality over the continental United States—A NASA unified WRF (NU-WRF) model study. *Atmospheric Chemistry and Physics*, *13*(13), 6207–6226. https://doi.org/10.5194/acp-13-6207-2013
Tracy, C. R., van Berkum, F. H., Tsuji, J. S., Stevenson, R. D., Nelson, J. A., Barnes, B. M., & Huey, R. B. (1984). Errors resulting from linear approximations in energy balance equations. *Journal of Thermal Biology*, *9*(4), 261–264. https://doi.org/10.1016/0306-4565(84)90006-8
Wang, D., & Hejazi, M. (2011). Quantifying the relative contribution of the climate and direct human impacts on mean annual streamflow in the contiguous United States. *Water Resources Research*, *47*, 1080–1016. https://doi.org/10.1029/2010WR010283
Wang, L., Huang, M., & Li, D. (2020). Where are white roofs more effective in cooling the surface? *Geophysical Research Letters*, *47*, 1–29. https://doi.org/10.1029/2020GL087853

Wang, P., Li, D., Liao, W., Rigden, A., & Wang, W. (2019). Contrasting evaporative responses of ecosystems to heatwaves traced to the opposing roles of vapor pressure deficit and surface resistance. *Water Resources Research*, *55*, 4550, 2019WR024771–4563. https://doi.org/10.1029/2019WR024771

Wilson, K. B., Baldocchi, D. D., Aubinet, M., Berbigier, P., Bernhofer, C., Dolman, H., et al. (2002). Energy partitioning between latent and sensible heat flux during the warm season at FLUXNET sites. *Water Resources Research*, *38*. https://doi.org/10.1029/2001WR000989

Xu, X., Yang, D., Yang, H., & Lei, H. (2014). Attribution analysis based on the Budyko hypothesis for detecting the dominant cause of runoff decline in Haihe basin. *Journal of Hydrology*, *510*(C), 530–540. https://doi.org/10.1016/j.jhydrol.2013.12.052

Yang, H., & Yang, D. (2011). Derivation of climate elasticity of runoff to assess the effects of climate change on annual runoff. *Water Resources Research*, *47*. https://doi.org/10.1029/2010WR009287

Zeng, Z., Piao, S., Li, L. Z. X., Zhou, L., Ciais, P., Wang, T., et al. (2017). Climate mitigation from vegetation biophysical feedbacks during the past three decades. *Nature Climate Change*, *7*(6), 432–436. https://doi.org/10.1038/nclimate3299

Zhang, S., Yang, H., Yang, D., & Jayawardena, A. W. (2016). Quantifying the effect of vegetation change on the regional water balance within the Budyko framework. *Geophysical Research Letters*, *43*, 1140–1148. https://doi.org/10.1002/2015GL066952

Zhao, C., Liu, B., Piao, S., Wang, X., Lobell, D. B., Huang, Y., et al. (2017). Temperature increase reduces global yields of major crops in four independent estimates. *Proceedings of the National Academy of Sciences*, *114*(35), 9326–9331. https://doi.org/10.1073/pnas.1701762114

Zhao, L., Lee, X., & Schultz, N. M. (2017). A wedge strategy for mitigation of urban warming in future climate scenarios. *Atmospheric Chemistry and Physics*, *17*(14), 9067–9080. https://doi.org/10.5194/acp-17-9067-2017

Zhao, L., Lee, X., Smith, R. B., & Oleson, K. (2014). Strong contributions of local background climate to urban heat islands. *Nature*, *511*(7508), 216–219. https://doi.org/10.1038/nature13462